

A Neural Network Potential Energy Surface and Quantum Dynamics Study of $\text{Ca}(^1\text{S}) + \text{H}_2(v_0 = 0, j_0 = 0) \rightarrow \text{CaH} + \text{H}$ Reaction

Hanghang Chen, Ye Mao, Zijiang Yang,* and Maodu Chen*

Cite This: *ACS Omega* 2024, 9, 30804–30812

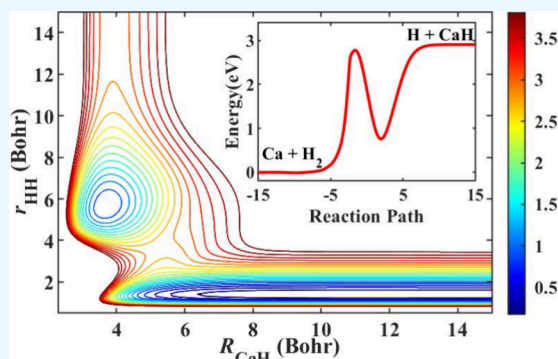
Read Online

ACCESS |

Metrics & More

Article Recommendations

ABSTRACT: The reactive collision between Ca and H_2 molecules has attracted great interest experimentally due to the key role of the product CaH molecule in the field of astrophysics and cold molecules. However, quantum dynamics calculations for this system have not been reported due to the lack of a global potential energy surface (PES). Herein, a globally accurate PES of the ground-state CaH_2 is developed by combining 11365 high-level ab initio points and permutation invariant polynomial neural network method. Based on the newly constructed PES, the state-to-state quantum dynamics calculations for the $\text{Ca}(^1\text{S}) + \text{H}_2(v_0 = 0, j_0 = 0) \rightarrow \text{CaH} + \text{H}$ reaction are carried out using the time-dependent wave packet method. The dynamic results reveal that the reaction follows the complex-forming mechanism near the reactive threshold, whereas both the indirect insertion mechanism and direct abstraction mechanism have effects at higher collision energies. The newly constructed PES can be used to further study the influence of isotope substitution, rovibrational excitation, and spatial orientation of reactant molecules on reaction dynamics.



1. INTRODUCTION

Calcium monohydride has attracted significant attention in the fields of quantum chemistry, molecular spectroscopy, and astrophysics. One reason for this is the importance of the spectroscopic characteristics of the CaH molecule in simulating and analyzing astrophysical phenomena, given its prevalence in various interstellar environments.^{1,2} Commencing with Mulliken's inaugural spectroscopic study of the CaH molecule in 1925,³ extensive studies for electronic states,^{4–7} ro-vibrational states,^{7–9} and key properties such as the permanent electric dipole moment^{10,11} of the CaH molecule have been carried out. On the other hand, the CaH molecule has a relatively simple ground-state hyperfine level structure, shorter excited-state lifetimes, and highly diagonal Franck–Condon factors for its $X^2\Sigma^+ - A^2\Pi_{1/2}$ and $B^2\Sigma^+ - A^2\Pi_{1/2}$ transitions,^{12,13} making it well-suited for laser cooling of cold molecules and magneto-optical trapping.

As a pathway for the generation of the CaH molecule, the reactive collision between Ca and H_2 molecules has been extensively studied both experimentally and theoretically. Experimentally, Lin et al.¹⁴ first reported the rotational state distribution and energy disposal of the CaH product of the $\text{Ca}(^1\text{P}) + \text{H}_2$ reaction by analyzing the laser-induced fluorescence spectra of the product molecule CaH. The result shows that the total available energy of 2893 cm^{-1} is allocated to the rotational state, vibrational state, and translation state, corresponding to energies of 552 ± 50 , 955 ± 38 , and $1342 \pm 88 \text{ cm}^{-1}$ and concluded that the reaction is biased toward

collinear geometric collisions. Using pump–probe technology, they also observed that the vibrational excitation of H_2 enlarges the H_2 bond distance and thus facilitates the $\text{Ca}(^1\text{P}) + \text{H}_2$ reaction without opening an additional pathway.¹⁵ Furthermore, the study on the $\text{Ca}(^1\text{D}) + \text{H}_2$ reaction revealed that the reaction has a preference for a near C_{2v} collision configuration,¹⁶ and the allocated proportions of product available energy for rotation, vibration, and translation are 0.36 ± 0.05 , 0.28 ± 0.04 , and 0.36 ± 0.05 , respectively.¹⁷ Theoretically, Lee et al.¹⁸ calculated six $^1A'$ potential energy surfaces (PESs) of the $\text{Ca} + \text{H}_2$ reaction system by using an effective-core potential and a core-polarization potential for Ca. They also conducted a simple analysis of the possible reaction paths through the wave functions.

Typically, rigorous quantum-mechanical calculations on a global high-precision PES are the most reliable means to obtain accurate dynamics results and mechanisms of molecular reactions.^{19,20} However, the previous PES of the CaH_2 system was mainly used to calculate the equilibrium configuration and vibration mode²¹ and did not include the asymptotic region

Received: April 10, 2024

Revised: June 12, 2024

Accepted: June 18, 2024

Published: July 2, 2024



that the reaction can access. Therefore, it is crucial to construct a global high-precision PES to calculate the dynamic results for the CaH₂ system. Despite much attention having been paid to the CaH₂ system, to the best of our knowledge, detailed quantum dynamics results of the Ca + H₂ reaction have not been reported.

In this work, a high-fidelity global PES for the ground-state CaH₂ is constructed based on a large number of high-level ab initio points and permutation invariant polynomial neural network (PIP-NN)^{22,23} method. Based on this new PES, the state-to-state quantum dynamics calculations for the Ca + H₂ ($v_0 = 0, j_0 = 0$) → CaH + H reaction are performed using the time-dependent wave packet (TDWP) method. The dynamic results of the reaction, including the reaction probabilities, the product quantum-state distribution, and the differential cross section (DCS), are calculated to thoroughly investigate and analyze the reaction mechanism. The rest of the paper is organized as follows: Section 2 gives a brief introduction to ab initio calculations, PES fitting, and quantum dynamical calculation methods. In Section 3, we first describe the topographic characteristics of the ground-state CaH₂ PES in detail and then discuss the microscopic mechanism of the title reaction. Finally, Section 4 presents the conclusions of this work.

2. THEORETICAL METHODS AND COMPUTATIONAL DETAILS

2.1. Ab Initio Calculations. The single-point energy of the ground-state (1¹A') CaH₂ is calculated at the internally contracted multireference configuration interaction (icMRCI)^{24,25} level with the Davidson correction (+Q), and cc-pV5Z²⁶ and def2-QZVP²⁷ basis sets are adopted for H and Ca, respectively. The molecular orbitals are optimized by the complete active space self-consistent field (CASSCF) calculations.²⁸ In the CASSCF calculations, the four valence electrons are included in 14 active orbitals (11a' + 3a''), corresponding to the 1s, 2s, and 2p orbitals of H and 4s, 3d, and 4p orbitals of the Ca atom. Nine orbitals (7a' + 2a'') are closed, which are related to 1s, 2s, 2p, 3s, and 3p orbitals of the Ca atom. The number of external orbitals is 143 (91a' + 52a''). The abovementioned choice of the CAS is determined by a number of tests that can ensure the convergence of most molecular configurations on the premise of high accuracy and acceptable computational cost. A mass of molecular geometries within C_s symmetry over a great range of space is selected to ensure that the fitted PES can entirely cover the dynamics-relevant regions. In Jacobi coordinates, the symmetrical configuration of Ca–H₂ is constructed by $0.8 \leq R_{\text{HH}}/a_0 \leq 20.0$, $0.1 \leq R_{\text{Ca-HH}}/a_0 \leq 30.0$, $0 \leq \theta \leq \pi/2$, and the configuration of H–CaH is defined by $2.6 \leq R_{\text{CaH}}/a_0 \leq 20.0$, $0.1 \leq R_{\text{H-CaH}}/a_0 \leq 16.0$, $0 \leq \theta' \leq \pi$. In this work, the ab initio calculations are carried out by utilizing the Molpro 2012 program.²⁹

2.2. PES Fitting with Neural Networks. In recent years, there has been increasing attention on representing molecular PESs by machine learning technology.^{23,30–37} Among those algorithms, the artificial NN model features high fitting accuracy and strong generalization performance and has become the most popular method in constructing reactive PESs of small systems. In this work, the back-propagation NN method is used to map the global ground-state CaH₂ PES. To ensure the fitted PES satisfies the exchange symmetry of the two same hydrogen atoms, the permutation invariant

polynomials^{22,23} are constructed by the bond length between two atoms as the input of NN, and the output layer is the corresponding normalized potential energy value. The input and output are connected by two hidden layers with 12 neurons. The hyperbolic tangent function is used as the transfer function φ in the 1–2 and 2–3 layers, and the 3–4 layer is lined by the linear function. The final analytical expansion of the fitted PES can be presented as

$$V_{\text{fit}} = \varphi^{(3)}(b_1^{(3)}) + \sum_{i=1}^{12} w_{i1}^{(3)} \varphi^{(2)}(b_i^{(2)}) + \sum_{j=1}^{12} w_{ji}^{(2)} \varphi^{(1)}(b_j^{(1)} + \sum_{k=1}^3 w_{kj}^{(1)} I_k) \quad (1)$$

where the connecting weights w and biases b between adjacent layers in a neural network are iteratively optimized using the Levenberg–Marquardt algorithm.³⁸ The mean squared error as a cost function for evaluating the training performance can be expressed as

$$\text{RMSE} = \sqrt{\frac{1}{N} \sum_{n=1}^N (E_n^{\text{ab initio}} - E_n^{\text{fitting}})^2} \quad (2)$$

2.3. Time-Dependent Wave Packet Method. Theoretically, the most reliable means to elucidate the reaction mechanism by dynamic results is to perform state-to-state dynamic calculations based on a globally accurate PES using an efficient quantum dynamic method. The TDWP method, widely acknowledged for its efficacy in the meticulous examination of reactive scattering, has been extensively utilized in various atom–diatom systems.^{39–44} The subsequent description provided an abbreviated overview of the TDWP method, and further intricate details can be referenced in the provided literature.^{45–48}

In the reactant Jacobi coordinates, the Hamiltonian of the Ca + H₂ system is written as

$$\hat{H} = -\frac{\hbar^2}{2\mu_R} \frac{\partial^2}{\partial R^2} + \frac{(\hat{J} - \hat{j})^2}{2\mu_R R^2} + \hat{h}(r) + \hat{V}(R, r, \theta) \quad (3)$$

with

$$\hat{h}(r) = -\frac{\hbar^2}{2\mu_r} \frac{\partial^2}{\partial r^2} + \frac{\hat{j}^2}{2\mu_r r^2} + V_0(r) \quad (4)$$

where J and j are the total angle momentum of the CaH₂ system and the rotational angular momentum of H₂ molecules, respectively. μ_R and μ_r are the reduced masses of the R and r radial coordinates. $\hat{V}(R, r, \theta)$ is the atom–diatom interaction potential excluding the diatom reference potential energy $V_0(r)$.

The total wave function in the body-fixed (BF) representation can be expanded in terms of the translational–vibrational–rotational basis as

$$\Psi^{JM\epsilon}(R, r, \theta) = \sum_{nvjK} F_{nvjK}^{JM\epsilon} D_{MK}^{J\epsilon}(\Omega) u_n(R) \phi_v(r) y_{jK}(\theta) \quad (5)$$

where ϵ is the parity of the system. M and K denote the projection of J on the space-fixed (SF) z axis and the BF z axis, respectively. $D_{MK}^{J\epsilon}(\Omega)$ is the parity-adapted normalized Wigner rotation matrix that only depends on Euler angles Ω . In this work, Sinc-DVR, PO–DVR, and Gauss–Legendre quadrature

are applied to Jacobi coordinates R , r , and θ to obtain the Hamiltonian matrix. In addition, an improved L-shaped grid method⁴⁷ recently introduced is applied to improve the efficiency of numerical calculation. The primary strategy of this method is to decompose the total wave function into the interaction region wave function and the asymptotic region wave function which use different numbers of rovibrational basis sets.

On the SF representation, the initial wave packet with a definite initial state (v_0, j_0, l_0) is prepared in the reactant asymptote as

$$\Psi_{v_0 j_0 l_0}^{JM\epsilon}(t=0) = G(R)\phi_{v_0 j_0}(r)|JMj_0 l_0 \epsilon\rangle \quad (6)$$

where $G(R)$ is a Gaussian function with the position R , $\phi_{v_0 j_0}(r)$ is the eigenfunction of diatom Hamiltonian eq 4 corresponding to the initial ro-vibrational state, and $|JMj_0 l_0 \epsilon\rangle$ is the total angular momentum eigenfunction.

The second-order split operator method⁴⁹ is employed to propagate wave packets. In order to avoid the reflection of the wave packet from the grid edges during the propagation, the absorption potential along r and R coordinates is constructed as follows:

$$D(x) = \begin{cases} \exp\left[-\Delta_t \cdot C_a \cdot \left(\frac{x - x_a}{x_b - x_a}\right)^2\right], & x_a \leq x \leq x_b \\ \exp\left[-\Delta_t \cdot C_b \cdot \left(\frac{x - x_b}{x_{\text{end}} - x_b}\right)^2\right] \\ \quad \times \exp(-\Delta_t \cdot C_a), & x_b < x \leq x_{\text{end}} \end{cases} \quad (7)$$

where C_a and C_b are the strength of absorbing potential. x_a , x_b , and x_{end} represent the starting and ending positions of absorbing potential.

The time-independent scattering wave function at the product asymptotic is obtained by the Fourier transform of the time-dependent wave function at each time step. Finally, the state-to-state S -matrix element is extracted by using the reactant-coordinate-based (RCB) method.^{50,51} Based on the S -matrix, the state-to-state reaction probability is calculated by

$$P_{v'j' \leftarrow v_0 j_0}^J = \frac{1}{2j_0 + 1} \sum_{K, K_0} |S_{v'j'K \leftarrow v_0 j_0 K_0}^J|^2 \quad (8)$$

where v' and j' are the product vibrational and rotational states, respectively. By summing over all relevant total angular momentum quantum numbers J , we can obtain the state-to-state integral cross sections (ICSS)

$$\sigma_{v'j' \leftarrow v_0 j_0} = \frac{\pi}{(2j_0 + 1)k_{v_0 j_0}^2} \sum_K \sum_{K_0} \sum_J (2J + 1) |S_{v'j'K \leftarrow v_0 j_0 K_0}^J|^2 \quad (9)$$

in which $k_{v_0 j_0} = \sqrt{2\mu_R E_c}$ is the wave vector in the entrance channel and E_c is the collision energy. The DCSs can be calculated as

$$\frac{d\sigma_{v'j' \leftarrow v_0 j_0}(\vartheta, E)}{d\Omega} = \frac{1}{(2j_0 + 1)} \sum_K \sum_{K_0} \left| \frac{1}{2ik_{v_0 j_0}} \sum_J (2J + 1) d_{KK_0}^J(\vartheta) S_{v'j'K \leftarrow v_0 j_0 K_0}^J \right|^2 \quad (10)$$

where $d_{KK_0}^J(\vartheta)$ represents the reduced Wigner matrix, and ϑ expresses the scattering angle.

3. RESULTS AND DISCUSSION

During the NN fitting, overfitting problems are often encountered, especially for the long-range potential. To avoid the overfitting behavior, the cross-validation scheme is applied, namely, the 11365 ab initio data are selected to participate in the PES fitting, which is randomly classified into 90% training set and 10% testing set. Atom–diatom Jacobi coordinates are used to generate energy points. The selection of the starting point must fully cover the entire coordinate space to ensure the quality of asymptotic channels and dynamical calculations. Second, considering the complexity of features within the interaction region, a denser energy point distribution is adopted in this region to improve the accuracy of PES. The training process is stopped when the error of the training set declines slowly or the error of the test set starts to rise, which usually suggests that the overfitting behavior occurs. Figure 1

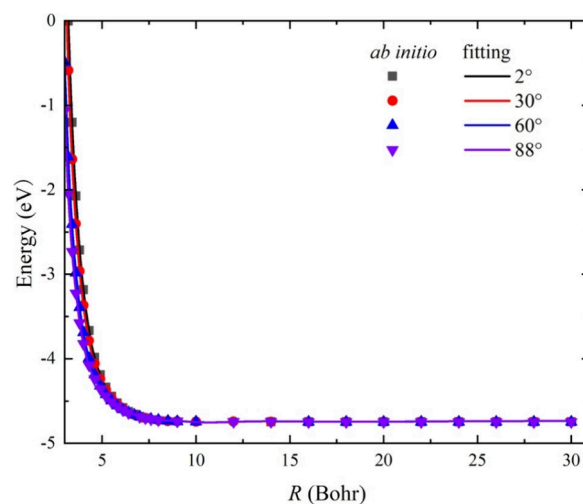


Figure 1. Comparison of ab initio data and the corresponding values obtained on the PIP-NN PES in a long-range of the reactant channel as a function of $R_{\text{Ca-HH}}$ at four Jacobi angles ($\theta = 2^\circ, 30^\circ, 60^\circ$ and 88°) for the bond length of HH fixed at $1.401 a_0$.

presents a comparison between the long-range potential energy values obtained on the new PES and the corresponding ab initio data along the radial coordinate at four selected Jacobi angles $\theta = 2^\circ, 30^\circ, 60^\circ$ and 88° , where the bond length of HH is fixed at its equilibrium distance ($1.401 a_0$). It can be seen that the fitting potentials are very smooth, in good agreement with the original ab initio calculations for each angle. The overall root-mean-square error of the global PES is only 6.245 meV, and the database with an absolutely fitting error less than 0.010 eV can reach 98.8%. This suggests that the constructing PES is globally accurate and suitable for carrying out the reaction dynamics calculations. As shown in Figure 2, the fitting two-body potential energy curves (PECs) of the ground state $\text{H}_2(X^1\Sigma_g^+)$ and $\text{CaH}(X^2\Sigma^+)$ molecules are in excellent agreement with each ab initio point. To further demonstrate the accuracy of the two-body potentials, Table 1 displays the spectroscopic constants of the two diatomic molecules determined on the analytical PECs, which exhibit good agreement with the corresponding experimental data.^{52,53}

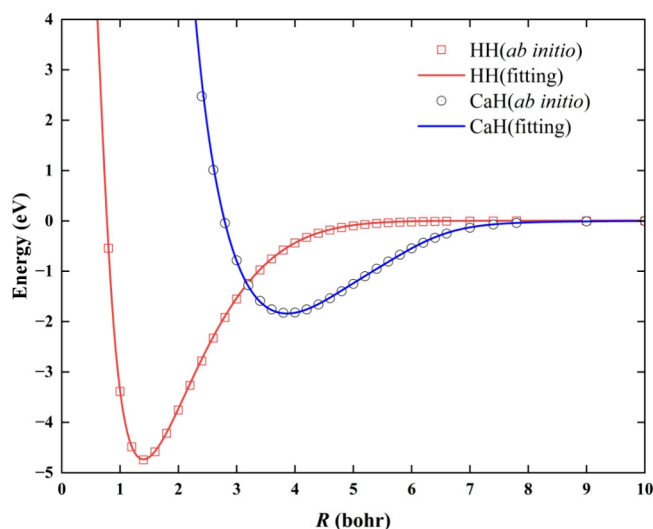


Figure 2. Comparison of the ab initio data and the NN fitting results of the PECs of H_2 ($X^1\Sigma_g^+$) and $\text{CaH}(X^2\Sigma^+)$.

Table 1. Molecular Constants of $\text{H}_2(X^1\Sigma_g^+)$ and $\text{CaH}(X^2\Sigma^+)$

	r_e (Å)	D_e (eV)	ω_e (cm^{-1})	$\omega_e x_e$ (cm^{-1})
$\text{H}_2(X^1\Sigma_g^+)$				
PIP-NN PES ^a	0.741	4.724	4401.8	120.8
experimental data ^b	0.741	4.747	4401.2	121.3
$\text{CaH}(X^2\Sigma^+)$				
PIP-NN PES ^a	2.044	1.828	1251.2	23.6
experimental data	2.002 ^c	1.788 ^b	1298.3 ^c	19.2 ^c

^aObtained from the analytical PECs. ^bFrom to ref 52. ^cExperimental values taken from ref 53.

Therefore, the presented PES are sufficiently accurate for representing the rovibrational states of reactant and product.

Contour maps of the ground-state CaH_2 PES at four different configurations are shown in Figure 3, where the energy is set as zero at the dissociation limit of the $\text{Ca} + \text{H}_2$ asymptotic region. Panels (a) and (b) depict the topographies of the CaH_2 PES with $\text{H}-\text{Ca}-\text{H}$ angles of 90° and 180° , respectively. The PES exhibits outstanding exchange symmetry, and a potential well structure with a depth of 2.09 eV is observed at $R_1 = R_3 = 3.84 a_0$ for the bond angle of 90° . A similar well is also presented at $R_1 = R_3 = 3.95 a_0$ for the bond angle of 180° , corresponding to the $D_{\infty h}$. The same characteristic is present on the ground-state PES of both BeH_2 and MgH_2 , and the depth of the potential well relative to the reactant asymptotic region decreases as the mass of the alkaline earth metal atom increases.^{54–56} Furthermore, the topography exhibits minimal changes as the bending angle increases under this configuration. Panel (c) illustrates the morphology of the PES at C_{2v} symmetry based on the reactant-Jacobi coordinate, where a saddle point is observed at a bond length of $R = 3.71 a_0$ and $r = 2.82 a_0$. Moreover, a deep potential well emerges when the Ca atom approaches the midpoint between two H atoms. As shown in Figure 3d, the global minimum energy point is located at the asymptotic region of the reactant channel. The energy level within the product channel significantly surpasses that of the reactant channel, signifying that the progression of the title reaction necessitates a substantial infusion of energy.

Contour plots of the potential energy of the atom (Ca or H) moving around the diatom molecules (H_2 or CaH) are

displayed in Figure 4, where the molecules are fixed at the corresponding equilibrium bond lengths. As shown in Figure 4a, evident repulsion between the Ca atom and H_2 molecule makes it challenging to initiate the title reaction, reflecting a common characteristic in ground-state reactions between alkali-earth metal atoms and the H_2 molecule. Different from the situation of Figure 4a, attractive interactions emerge, as shown in Figure 4b, as the H atom moves around the CaH molecule, and the well around the Ca atom is deeper and broader than the well around another H atom. The potential well on the left is located in the structure where the Ca atom is between two H atoms with a bond length of about 8 Bohr, which corresponds to the well shown in Figure 3b. Furthermore, it can be seen from Figures 3 and 4 that the potential energy curves derived from the newly constructed PES are notably smooth, indicating that there is no overfitting during the NN training.

To enhance the clarity of the features associated with the title reaction within this latest PES, Figure 5 depicts both the global minimum energy path (MEP) and the MEPs at four $\text{Ca}-\text{H}-\text{H}$ angles ($45^\circ, 80^\circ, 90^\circ, 135^\circ$) for the $\text{Ca}(^1\text{S}) + \text{H}_2 \rightarrow \text{CaH} + \text{H}$ reaction. Here, the reaction coordinate is defined as the difference between R_{HH} and R_{CaH} distances, and $\theta_{\text{Ca}-\text{H}-\text{H}}$ is the bending angle between R_{HH} and R_{CaH} . It can be discerned from the MEPs that the titled reaction is a markedly endothermic process, requiring an energy absorption of 2.91 eV. The global MEP shows an extremely deep potential well with energy as low as 0.17 eV in the reaction path, which corresponds to the potential well structure shown in Figure 3b. In this structure, the Ca atom is positioned at the midpoint between two H atoms, with an R_{CaH} distance of $3.96 a_0$. For the MEPs at different angles, it is evident that the potential well only exists in the reaction path at small approach angles ($\theta_{\text{Ca}-\text{H}-\text{H}} < 80^\circ$). After accounting for the vibrational zero-point energies of the H_2 and CaH molecules, the title reaction is an endothermic reaction with an absorption energy of 2.71 eV.

In order to obtain accurate and detailed dynamical information, we conducted dynamical calculations for the $\text{Ca} + \text{H}_2$ ($v_0 = 0, j_0 = 0$) $\rightarrow \text{CaH} + \text{H}$ reaction within the energy range of 2.5 to 4.0 eV. In the TDWP calculation, the total angular momentum J is calculated from 0 to 78, and all Coriolis couplings are considered. The primary numerical parameters in the calculation after a large number of convergence tests are given in Table 2. The collision energy dependence of the total reaction probabilities for the $\text{Ca}(^1\text{S}) + \text{H}_2$ ($v_0 = 0, j_0 = 0$) $\rightarrow \text{CaH} + \text{H}$ reaction at four different total angular momentum J (0, 20, 40, 60) are depicted in Figure 6a. For $J = 0$, there is a reaction threshold whose magnitude is consistent with the endothermicity calculated from the PES. The reaction threshold increases with the increase of J due to the role of the centrifugal potential term in eq 3. In addition, a number of significant oscillating peaks are found in the reaction probability curves for small J , which can be attributed to the formation of long-lived complexes in the potential well. These oscillations gradually weaken as the J value increases until it disappears on the curve $J = 60$. The domination of resonance caused by the long-lived complexes is consistent with the insertion reaction mechanism, which is foretold in the reaction path diagram of Figure 5. The total ICS for the title reaction is also shown in Figure 6b. It is obvious that the total ICS increases monotonically with the collision energy, which is a typical characteristic of a strong endothermic reaction.

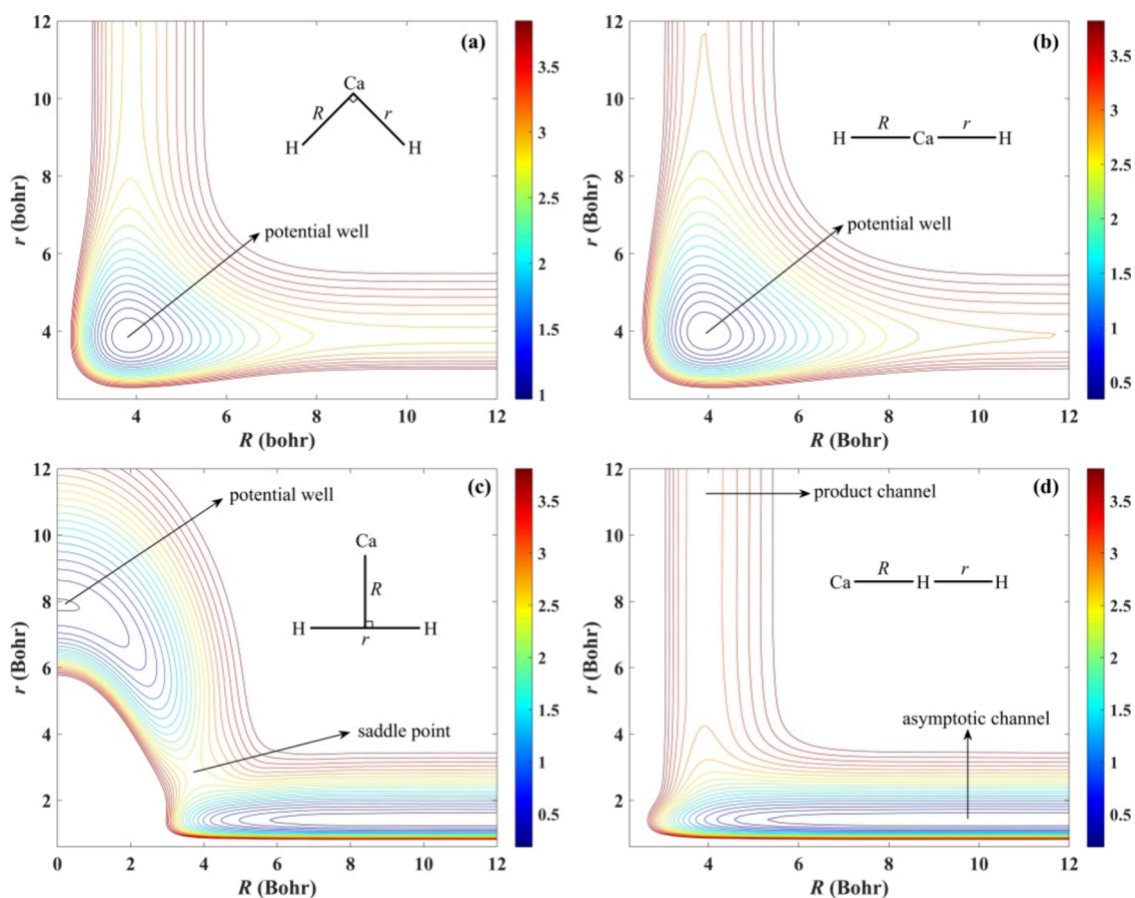


Figure 3. Contour plots of the ground-state CaH_2 PES (a) for the bending angle between R_{HCa} and R_{CaH} fixed at 90° , (b) for the bending angle between R_{HCa} and R_{CaH} fixed at 180° (D_{ohh} symmetry), (c) for the reactant-Jacobi coordinate $R_{\text{Ca-HH}}$ and r_{HH} with the angle $\theta = 90^\circ$, and (d) for the Ca-H-H angle fixed at 180° .

The revelation of reaction mechanisms and the control of reaction processes are greatly facilitated by studying the vibrational behavior of products.^{57,58} The vibrational–rotational distribution of the product molecule calculated by the TDWP method at the collision energy of 3.2, 3.5, 3.8, and 4.0 eV is shown in Figure 7. It can be seen that with the increase of collision energy, the opening of more product channels leads to a broader distribution of the product vibrational–rotational states. In addition, the product vibrational state distribution is depicted in the figure with the orange dotted line. The results show that the product molecule mainly occupies lower vibrational states near the reaction threshold. As the collision energy increases, the vibrational states of the CaH product show population inversion distributions. This dynamical behavior is very common in many systems, such as $\text{Be} + \text{H}_2$ ⁵⁴ and $\text{F} + \text{HCl}$ reactions.^{58–60} The results reveal that the product molecule mainly occupies lower vibrational states and the dominant vibrational state changes from $v' = 0$ to $v' = 2$ as the collision energy increases. On the contrary, the results at different collision energies consistently indicate that the product molecule shows a preference for higher rotational states and the maximum distribution being at rotational state $j' = 20$. This rovibrational distribution characteristic is consistent with typical features of the insertion reaction mechanism. In contrast, the direct-abstraction reaction tends to be distributed in lower rotational states. Overall, the features observed in the figure further demonstrate that the reaction follows an

insertion reaction mechanism dominated by long-lived complexes.

DCS can provide a more detailed exploration of the reaction mechanism by offering the angular distribution of reaction products. For the direct abstraction reaction mechanisms, the products usually have a nonstatistical distribution and prefer to scatter in one direction. For the indirect insertion reaction mechanism, the adjustment time of the reaction is longer, which can eliminate the kinetic information of the initial reactants so that the products can be scattered in all directions and have a symmetric distribution of forward and backward scatterings. As shown in Figure 8, the DCSs of the $\text{Ca} + \text{H}_2$ ($v_0 = 0, j_0 = 0$) $\rightarrow \text{CaH} + \text{H}$ reaction as a function of scattering angle at several selected collision energies are presented. Almost symmetrical forward–backward scattering is found at low collision energy, which is consistent with the characteristics of complex formation reaction, confirming the indirect insertion reaction mechanism of $\text{Ca}(^1\text{S}) + \text{H}_2$ reaction when the collision energy is close to the reactive threshold. As the collision energy increases, the forward and backward scattering peaks become larger and broader. The backward scattering peak gradually intensifies with the increase of collision energy, indicating that the direct abstraction mechanism plays a role in the title reaction. Therefore, both the indirect insertion mechanism and direct abstraction mechanism have effects on the $\text{Ca}(^1\text{S}) + \text{H}_2$ reaction at high collision energies.

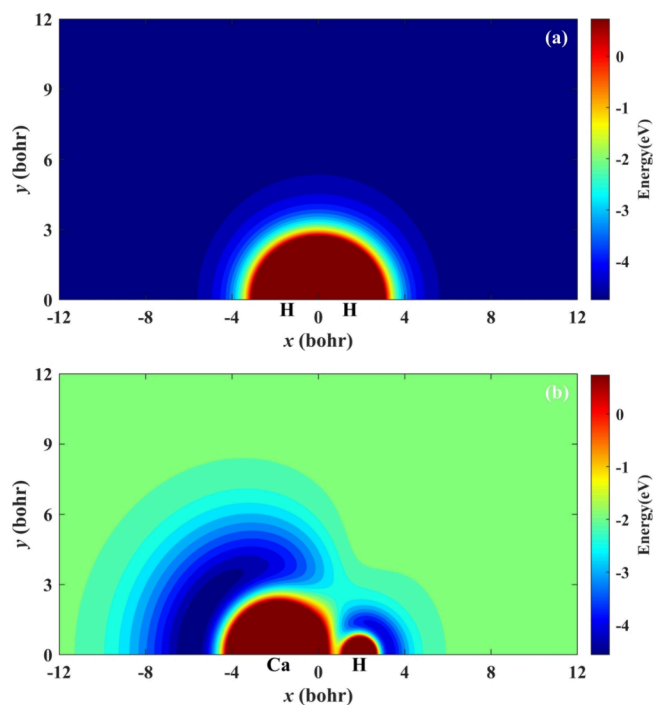


Figure 4. Contour plot of potential energy when (a) Ca atom moves around the H_2 molecule with the fixed bond length at 1.40 Bohr, and (b) H atom moves around the CaH molecule with the fixed bond length at 3.86 Bohr.

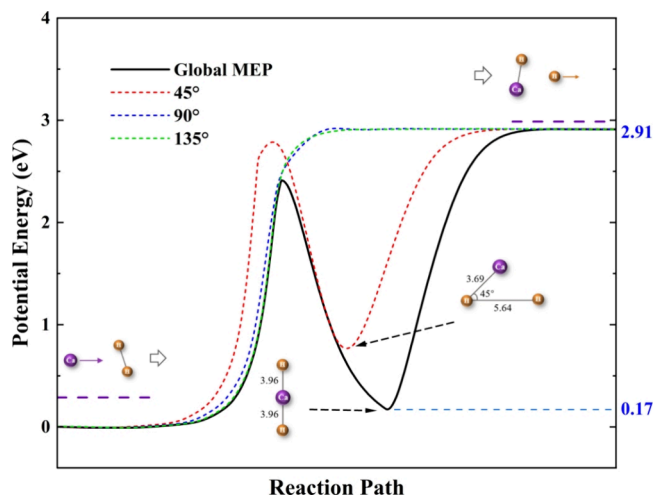


Figure 5. Global MEP and MEPs at four Ca–H–H angles (45° , 80° , 90° , 135°) of the $\text{Ca} + \text{H}_2 \rightarrow \text{CaH} + \text{H}$ reaction, where zero energy corresponds to the asymptotic energy of the $\text{Ca} + \text{H}_2$ reactant (the unit of bond length is Bohr).

4. CONCLUSIONS

In this work, a high-fidelity global ground-state CaH_2 PES is constructed using the PIP-NN scheme based on 11365 ab initio points calculated at the icMRCI + Q level, and cc-pV5Z and def2-QZVP basis sets are adopted for H and Ca, respectively. The PES can accurately reproduce the original ab initio data in each region, and the overall fitting RMSE of the mapped PES is only 6.245 meV. The topographic features of the PES are described in detail. The ground-state PES of CaH_2 exhibits a potential well structure with exchange symmetry, and the comparison with the results of BeH_2 and

Table 2. Numerical Parameters Used in the TDWP Calculations for $\text{Ca}(^1\text{S}) + \text{H}_2 (v_0 = 0, j_0 = 0) \rightarrow \text{CaH} + \text{H}$ Reaction^a

parameter	value
R	$R \in [0.1, 25.0]$, $N_R = 299$, $N_R^{\text{int}} = 149$
r	$r \in [0.01, 25.0]$, $\nu_{\text{int}} = 199$, $\nu_{\text{Asy}} = 15$
rotational basis	$j_{\text{int}} = 169$, $j_{\text{Asy}} = 39$
initial wave packet	$R_c = 18.0$, $\delta = 0.32$, $E_c = 3.8$ eV
absorbing potential	R : $C_a = 0.06$, $C_b = 0.12$, $R_a = 20.0$, $R_b = 24.0$ r : $C_a = 0.06$, $C_b = 0.15$, $r_a = 20.0$, $r_b = 24.0$
propagation time	$T_{\text{tot}} = 30,000$, $\Delta_t = 15$
matching plane	$R_0' = 12.0$

^aAtomic units are used if not otherwise stated.

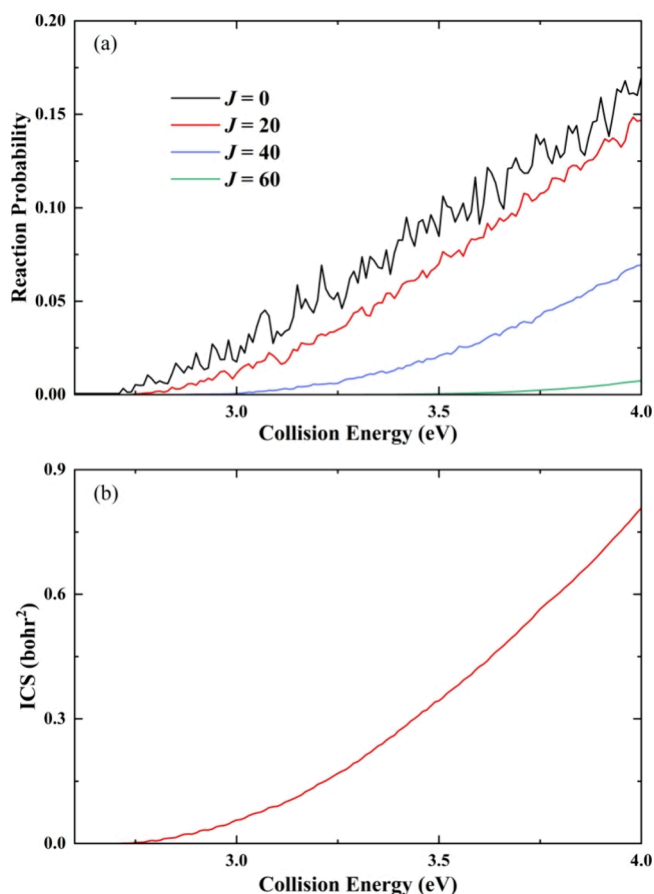


Figure 6. (a) Reaction probabilities with four different total angular momenta ($J = 0, 20, 40, 60$) and (b) total ICS for the $\text{Ca} + \text{H}_2 (v_0 = 0, j_0 = 0) \rightarrow \text{CaH} + \text{H}$ reaction as a function of collision energy.

MgH_2 concludes that the depth of the potential well decreases with the increase of the atomic mass of alkaline earth metal.

Based on this new PES, state-to-state quantum dynamics calculations for the $\text{Ca} + \text{H}_2 (v_0 = 0, j_0 = 0) \rightarrow \text{CaH} + \text{H}$ reaction are performed using the TDWP method for understanding the microscopic mechanisms. Significant oscillating peaks in the reaction probability curves at small angular momenta suggest the formation of long-lived complexes in the potential well. The rovibrationally state-resolved ICSs present vibrationally cold and rotationally hot distribution. The total DCSs are forward–backward symmetric when the collision energy is slightly larger than the reactive threshold, while the backward scattering is more favorable at

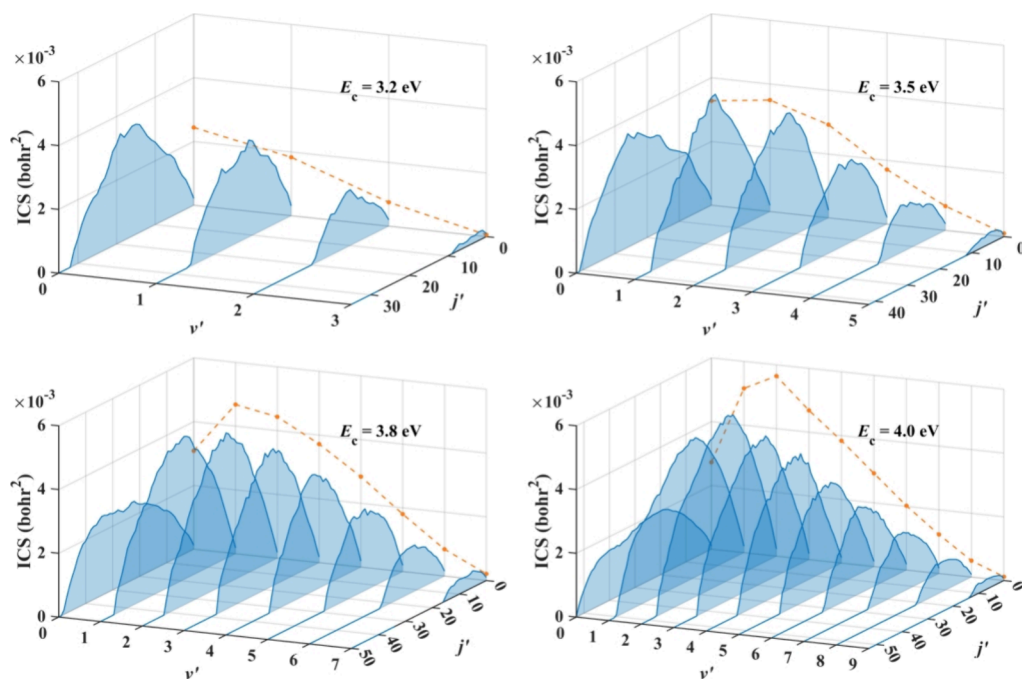


Figure 7. Product vibrational–rotational state distribution of the $\text{Ca} + \text{H}_2$ ($\nu_0 = 0, j_0 = 0$) \rightarrow $\text{CaH} + \text{H}$ reaction at four selected collision energies (3.2, 3.5, 3.8, and 4.0 eV). The orange dashed lines represent the relative distribution of the product vibration state.

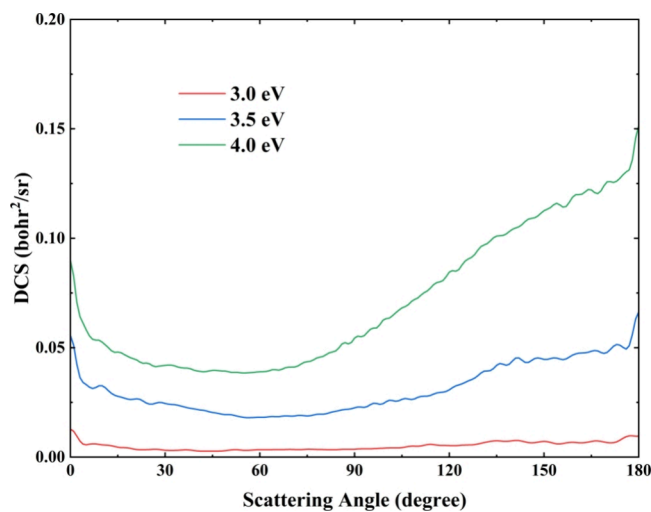


Figure 8. DCSs of the $\text{Ca} + \text{H}_2$ ($\nu_0 = 0, j_0 = 0$) \rightarrow $\text{CaH} + \text{H}$ reaction as a function of the scattering angle at several selected collision energies calculated by the TDWP method.

high collision energy. The dynamics results indicate that near the reactive threshold, the title reaction follows a complex-forming mechanism, whereas both the indirect insertion mechanism and the direct abstraction mechanism contribute to the $\text{Ca}(^1\text{S}) + \text{H}_2$ reaction at higher collision energies. Further dynamics studies for this reaction system, such as the effects of rovibrational excitations and isotopic substitutions of the H_2 molecule, can be performed on the presented PES, and the dynamics data calculated in this study would be of importance in the experimental studies on the title reaction.

AUTHOR INFORMATION

Corresponding Authors

Zijiang Yang – School of Physics and Electronic Technology, Liaoning Normal University, Dalian 116029, China; Email: yangzijiang@lnnu.edu.cn

Maodu Chen – Key Laboratory of Materials Modification by Laser, Electron, and Ion Beams (Ministry of Education), School of Physics, Dalian University of Technology, Dalian 116024, China; orcid.org/0000-0003-4909-7993; Email: mdchen@dlut.edu.cn

Authors

Hanghang Chen – Key Laboratory of Materials Modification by Laser, Electron, and Ion Beams (Ministry of Education), School of Physics, Dalian University of Technology, Dalian 116024, China; orcid.org/0000-0002-2453-0431

Ye Mao – Key Laboratory of Materials Modification by Laser, Electron, and Ion Beams (Ministry of Education), School of Physics, Dalian University of Technology, Dalian 116024, China

Complete contact information is available at:

<https://pubs.acs.org/10.1021/acsomega.4c03465>

Notes

The authors declare no competing financial interest.

ACKNOWLEDGMENTS

This work was supported by the National Natural Science Foundation of China (Grant No. 12374226).

REFERENCES

- (1) Lépine, S.; Scholz, R.-D. Twenty-three new ultracool subdwarfs from the sloan digital sky survey. *Astrophys. J.* **2008**, *681* (1), L33.
- (2) Barbuy, B.; Schiavon, R. P.; Gregorio-Hetem, J.; Singh, P. D.; Batalha, C. Intensity of CaH lines in cool dwarfs. *Astron. Astrophys., Suppl. Ser.* **1993**, *101*, 409–413.

- (3) Mulliken, R. S. A band of unusual structure probably due to a highly unstable calcium hydride molecule. *Phys. Rev.* **1925**, *25* (4), 509–522.
- (4) Habli, H.; Jellali, S.; Oujia, B. Electronic, structural and vibrational properties of calcium monohydride. *Phys. Scr.* **2020**, *95* (1), No. 015403.
- (5) Shayesteh, A.; Alavi, S. F.; Rahman, M.; Gharib-Nezhad, E. Ab initio transition dipole moments and potential energy curves for the low-lying electronic states of CaH. *Chem. Phys. Lett.* **2017**, *667*, 345–350.
- (6) Ferreira, I. B.; Campos, C. T.; Jorge, F. E. All-electron basis sets augmented with diffuse functions for He, Ca, Sr, Ba, and lanthanides: application in calculations of atomic and molecular properties. *J. Mol. Model.* **2020**, *26* (5), 95.
- (7) Watanabe, K.; Yoneyama, N.; Uchida, K.; Kobayashi, K.; Matsushima, F.; Moriawaki, Y.; Ross, S. C. According theory and experiment in CaH: Laser-induced fluorescence study of new B/B'–X bands in the UV region. *Chem. Phys. Lett.* **2016**, *657*, 1–7.
- (8) Yadin, B.; Veness, T.; Conti, P.; Hill, C.; Yurchenko, S. N.; Tennyson, J. ExoMol line lists - I. The rovibrational spectrum of BeH, MgH and CaH in the $X^2\Sigma^+$ state. *Mon. Not. R. Astron. Soc.* **2012**, *425* (1), 34–43.
- (9) Watanabe, K.; Tani, I.; Kobayashi, K.; Moriawaki, Y.; Ross, S. C. Laser spectroscopic study of the B/B' $^2\Sigma^+ - X^2\Sigma^+(9-0)$, (10–0), (11–0) and (18–0) bands of CaH. *Chem. Phys. Lett.* **2018**, *710*, 11–15.
- (10) Chen, J.; Steimle, T. C. The permanent electric dipole moment of calcium monodeuteride. *J. Chem. Phys.* **2008**, *128* (14), 144312.
- (11) Fazil, N. M.; Prasanna, V. S.; Latha, K. V. P.; Abe, M.; Das, B. P. Electron correlation trends in the permanent electric dipole moments of alkaline-earth-metal monohydrides. *Phys. Rev. A* **2018**, *98* (3), No. 032511.
- (12) GharibNezhad, E.; Shayesteh, A.; Bernath, P. F. Fourier transform emission spectra of the $A^2\Pi X^2\Sigma^+$ and $B^2\Sigma^+ \rightarrow X^2\Sigma^+$ transitions of CaD. *J. Mol. Spectrosc.* **2012**, *281*, 47–50.
- (13) Liu, M.; Pauchard, T.; Sjödin, M.; Launila, O.; van der Meulen, P.; Berg, L. E. Time-resolved study of the $A^2\Pi$ state of CaH by laser spectroscopy. *J. Mol. Spectrosc.* **2009**, *257* (1), 105–107.
- (14) Liu, D.-K.; Chen, J.-J.; Nien, C.-F.; Lin, K.-C. Nascent rotational distribution and energy disposal of the CaH product in the reaction of $\text{Ca}(4s4p^1P_1) + \text{H}_2 \rightarrow \text{CaH}(X^2\Sigma^+) + \text{H}$. *J. Chem. Phys.* **1999**, *111* (11), 5277–5278.
- (15) Chen, J.-J.; Hsiao, M.-K.; Lin, K.-C. Influence of vibrational excitation on the nonadiabatic reactions of metal atoms with H_2 . *J. Chem. Phys.* **2005**, *123* (12), 121101.
- (16) Song, Y.-W.; Chen, J.-J.; Hsiao, M.-K.; Lin, K.-C.; Hung, Y.-M. Reaction pathway and potential barrier for the CaH product in the reaction of $\text{Ca}(4s4p^1P_1) + \text{H}_2 \rightarrow \text{CaH}(X^2\Sigma^+) + \text{H}$. *J. Chem. Phys.* **2004**, *120* (6), 2774–2779.
- (17) Lin, K.-C.; González Ureña, A. Dynamical and stereodynamical studies of alkaline-earth atom–molecule reactions. *Int. Rev. Phys. Chem.* **2007**, *26* (2), 289–352.
- (18) Kim, K. H.; Lee, H. S.; Lee, Y. S.; Jeung, G.-H. Potential energy surfaces for the photochemical reactions $\text{Ca}^* + \text{H}_2 \rightarrow \text{CaH} + \text{H}$. *J. Chem. Phys.* **2002**, *116* (2), 589–593.
- (19) Zhang, L.; Liu, D.; Yue, D.; Song, Y.; Meng, Q. Dynamics of $\text{H}(^2S) + \text{CH}(X^2\Pi)$ reactions based on a new $\text{CH}_2(X^3A'')$ surface via extrapolation to the complete basis set limit. *J. Phys. B-At. Mol. Opt.* **2020**, *53* (9), No. 09S202.
- (20) Fu, B.; Xu, X.; Zhang, D. H. A hierarchical construction scheme for accurate potential energy surface generation: An application to the $\text{F} + \text{H}_2$ reaction. *J. Chem. Phys.* **2008**, *129* (1), No. 011103.
- (21) Koput, J. Ab initio prediction of the potential energy surface and vibrational–rotational energy levels of calcium dihydride, CaH_2 . *J. Phys. Chem. A* **2005**, *109* (19), 4410–4414.
- (22) Braams, B. J.; Bowman, J. M. Permutationally invariant potential energy surfaces in high dimensionality. *Int. Rev. Phys. Chem.* **2009**, *28*, 577–606.
- (23) Jiang, B.; Guo, H. Permutation invariant polynomial neural network approach to fitting potential energy surfaces. *J. Chem. Phys.* **2013**, *139* (5), No. 054112.
- (24) Werner, H. J.; Knowles, P. J. An efficient internally contracted multiconfiguration–reference configuration interaction method. *J. Chem. Phys.* **1988**, *89* (9), 5803–5814.
- (25) Knowles, P. J.; Werner, H.-J. An efficient method for the evaluation of coupling coefficients in configuration interaction calculations. *Chem. Phys. Lett.* **1988**, *145* (6), 514–522.
- (26) Kendall, R. A.; Dunning, T. H., Jr.; Harrison, R. J. Electron affinities of the first-row atoms revisited. Systematic basis sets and wave functions. *J. Chem. Phys.* **1992**, *96* (9), 6796–6806.
- (27) Leininger, T.; Nicklass, A.; Küchle, W.; Stoll, H.; Dolg, M.; Bergner, A. The accuracy of the pseudopotential approximation: non-frozen-core effects for spectroscopic constants of alkali fluorides XF (X = K, Rb, Cs). *Chem. Phys. Lett.* **1996**, *255* (4), 274–280.
- (28) Knowles, P. J.; Werner, H.-J. An efficient second-order MC SCF method for long configuration expansions. *Chem. Phys. Lett.* **1985**, *115* (3), 259–267.
- (29) Werner, H.-J.; Knowles, P. J.; Knizia, G.; Manby, F. R.; Schütz, M. Molpro: a general-purpose quantum chemistry program package. *Wires Comput. Mol. Sci.* **2012**, *2* (2), 242–253.
- (30) Yang, T.; Li, A.; Chen, G. K.; Xie, C.; Suits, A. G.; Campbell, W. C.; Guo, H.; Hudson, E. R. Optical control of reactions between water and laser-cooled Be^+ ions. *J. Phys. Chem. Lett.* **2018**, *9* (13), 3555–3560.
- (31) Jiang, B.; Li, J.; Guo, H. High-fidelity potential energy surfaces for gas-phase and gas–surface scattering processes from machine learning. *J. Phys. Chem. Lett.* **2020**, *11* (13), 5120–5131.
- (32) Dai, J.; Krems, R. V. Interpolation and extrapolation of global potential energy surfaces for polyatomic systems by gaussian processes with composite kernels. *J. Chem. Theory Comput.* **2020**, *16* (3), 1386–1395.
- (33) Sugisawa, H.; Ida, T.; Krems, R. V. Gaussian process model of 51-dimensional potential energy surface for protonated imidazole dimer. *J. Chem. Phys.* **2020**, *153* (11), 114101.
- (34) Yang, Z.; Chen, H.; Chen, M. Representing globally accurate reactive potential energy surfaces with complex topography by combining Gaussian process regression and neural networks. *Phys. Chem. Chem. Phys.* **2022**, *24*, 12827–12836.
- (35) Yang, Z.; Yuan, J.; Wang, S.; Chen, M. Global diabatic potential energy surfaces for the BeH_2^+ system and dynamics studies on the $\text{Be}^+(^2P) + \text{H}_2(X^1\Sigma_g^+) \rightarrow \text{BeH}^+(X^1\Sigma^+) + \text{H}(^2S)$ reaction. *RSC Adv.* **2018**, *8* (40), 22823–22834.
- (36) Fu, B.; Zhang, D. H. Ab initio potential energy surfaces and quantum dynamics for polyatomic bimolecular reactions. *J. Chem. Theory Comput.* **2018**, *14* (5), 2289–2303.
- (37) Guan, Y.; Yang, S.; Zhang, D. H. Application of clustering algorithms to partitioning configuration space in fitting reactive potential energy surfaces. *J. Phys. Chem. A* **2018**, *122* (12), 3140–3147.
- (38) Hagan, M. T.; Menhaj, M. B. Training feedforward networks with the Marquardt algorithm. *IEEE Trans. Neural Netw.* **1994**, *5* (6), 989–993.
- (39) Yang, Z.; Chen, H.; Mao, Y.; Chen, M. A neural network potential energy surface and quantum dynamics studies for the $\text{Ca}^+(^2S) + \text{H}_2 \rightarrow \text{CaH}^+ + \text{H}$ reaction. *Phys. Chem. Chem. Phys.* **2022**, *24* (32), 19209–19217.
- (40) Chen, H.; Buren, B.; Yang, Z.; Chen, M. An effective approximation of Coriolis coupling in reactive scattering: application to the time-dependent wave packet calculations. *Phys. Chem. Chem. Phys.* **2023**, *25* (34), 22927–22940.
- (41) Buren, B.; Chen, M.; Sun, Z.; Guo, H. Quantum wave packet treatment of cold nonadiabatic reactive scattering at the state-to-state level. *J. Phys. Chem. A* **2021**, *125* (46), 10111–10120.
- (42) Mao, Y.; Chen, H.; Yang, Z.; Buren, B.; Chen, M. Quantum State-Resolved Nonadiabatic Dynamics of the $\text{H} + \text{NaF} \rightarrow \text{Na} + \text{HF}$ Reaction. *Chin. Phys. Lett.* **2024**, *41* (3), No. 038201.

- (43) Naskar, K.; Ghosh, S.; Adhikari, S.; Baer, M.; Sathyamurthy, N. Coupled three-dimensional quantum mechanical wave packet study of proton transfer in $\text{H}_2^+ + \text{He}$ collisions on accurate ab initio two-state diabatic potential energy surfaces. *J. Chem. Phys.* **2023**, *159* (3), No. 034302.
- (44) Adhikari, S.; Varandas, A. J. C. The coupled 3D wave packet approach for triatomic reactive scattering in hyperspherical coordinates. *Comput. Phys. Commun.* **2013**, *184* (2), 270–283.
- (45) Sun, Z.; Lee, S. Y.; Guo, H.; Zhang, D. H. Comparison of second-order split operator and Chebyshev propagator in wave packet based state-to-state reactive scattering calculations. *J. Chem. Phys.* **2009**, *130* (17), 174102.
- (46) Sun, Z.; Guo, H.; Zhang, D. H. Extraction of state-to-state reactive scattering attributes from wave packet in reactant Jacobi coordinates. *J. Chem. Phys.* **2010**, *132* (8), No. 084112.
- (47) Buren, B.; Chen, M. Stereodynamics-controlled product branching in the nonadiabatic $\text{H} + \text{NaD} \rightarrow \text{Na}(3s, 3p) + \text{HD}$ reaction at low temperatures. *J. Phys. Chem. A* **2022**, *126* (16), 2453–2462.
- (48) Marković, N.; Billing, G. D. The coupled three-dimensional wave packet approach to reactive scattering. *J. Chem. Phys.* **1994**, *100* (2), 1085–1093.
- (49) Feit, M. D.; Fleck, J. A.; Steiger, A. Solution of the Schrödinger equation by a spectral method. *J. Comput. Phys.* **1982**, *47* (3), 412–433.
- (50) Gomez-Carrasco, S.; Roncero, O. Coordinate transformation methods to calculate state-to-state reaction probabilities with wave packet treatments. *J. Chem. Phys.* **2006**, *125* (5), No. 054102.
- (51) Sun, Z.; Lin, X.; Lee, S.-Y.; Zhang, D. H. A reactant-coordinate-based time-dependent wave packet method for triatomic state-to-state reaction dynamics: application to the $\text{H} + \text{O}_2$ reaction. *J. Phys. Chem. A* **2009**, *113* (16), 4145–4154.
- (52) Huber, K. P.; Herzberg, G. Constants of diatomic molecules. In *Molecular Spectra and Molecular Structure: IV. Constants of Diatomic Molecules*; Huber, K. P.; Herzberg, G., Eds.; Springer US: Boston, MA, 1979; pp 8–689.
- (53) Shayesteh, A.; Ram, R. S.; Bernath, P. F. Fourier transform emission spectra of the $\text{A}^2\tilde{\text{I}}\text{X}^2\Sigma^+$ and $\text{B}^2\Sigma^+ \rightarrow \text{X}^2\Sigma^+$ band systems of CaH. *J. Mol. Spectrosc.* **2013**, *288*, 46–51.
- (54) Yang, Z.; Chen, M. A globally accurate potential energy surface and quantum dynamics calculations on the $\text{Be}(^1\text{S}) + \text{H}_2(v_0 = 0, j_0 = 0) \rightarrow \text{BeH} + \text{H}$ reaction. *Front. Phys.* **2022**, *10*, No. 1022222.
- (55) Li, A.; Li, J.; Guo, H. Quantum manifestation of roaming in $\text{H} + \text{MgH} \rightarrow \text{Mg} + \text{H}_2$: The birth of roaming resonances. *J. Phys. Chem. A* **2013**, *117* (24), 5052–5060.
- (56) Takayanagi, T.; Tanaka, T. Roaming dynamics in the $\text{MgH} + \text{H} \rightarrow \text{Mg} + \text{H}_2$ reaction: Quantum dynamics calculations. *Chem. Phys. Lett.* **2011**, *504* (4), 130–135.
- (57) Kornweitz, H.; Persky, A. Quasiclassical Trajectory Calculations for the Reactions $\text{F} + \text{HCl}$, $\text{F} + \text{HBr}$, and $\text{F} + \text{HI}$. *J. Phys. Chem. A* **2004**, *108* (1), 140–145.
- (58) Aoto, Y. A.; Köhn, A. Revisiting the $\text{F} + \text{HCl} \rightarrow \text{HF} + \text{Cl}$ reaction using a multireference coupled-cluster method. *Phys. Chem. Chem. Phys.* **2016**, *18* (44), 30241–30253.
- (59) Freixas-Lemus, V. M.; Martínez-Mesa, A.; Uranga-Piña, L. Quasi-classical trajectory study of $\text{F} + \text{HCl}$ reactive scattering at hyperthermal collision energies. *Eur. Phys. J. Spec. Top.* **2023**, *232* (12), 1945–1960.
- (60) Li, A.; Guo, H.; Sun, Z.; Klos, J.; Alexander, M. H. State-to-state quantum dynamics of the $\text{F} + \text{HCl}(v_i = 0, j_i = 0) \rightarrow \text{HF}(v_f, j_f) + \text{Cl}$ reaction on the ground state potential energy surface. *Phys. Chem. Chem. Phys.* **2013**, *15* (37), 15347–15355.